A general-purpose machine learning Pt interatomic potential for an accurate description of bulk, surfaces and nanoparticles

Jan Kloppenburg,[1, 2, *] Livia B. Pártay,[3] Hannes Jónsson,[4, 5] and Miguel A. Caro[1, 2, †]

[1]*Department of Electrical Engineering and Automation, Aalto University, 02150 Espoo, Finland*
[2]*Department of Chemistry and Materials Science, Aalto University, 02150 Espoo, Finland*
[3]*Department of Chemistry, University of Warwick, Coventry CV4 7AL, UK*
[4]*Faculty of Physical Sciences, University of Iceland, VR-III, 107 Reykjavík, Iceland*
[5]*Department of Applied Physics, Aalto University, FI-00076 Espoo, Finland*
(Dated: March 14, 2023)

A Gaussian approximation machine learning interatomic potential for platinum is presented. It has been trained on DFT data computed for bulk, surfaces and nanostructured platinum, in particular nanoparticles. Across the range of tested properties, which include bulk elasticity, surface energetics and nanoparticle stability, this potential shows excellent transferability and agreement with DFT, providing state-of-the-art accuracy at low computational cost. We showcase the possibilities for modeling of Pt systems enabled by this potential with two examples: the pressure-temperature phase diagram of Pt calculated using nested sampling and a study of the spontaneous crystallization of a large Pt nanoparticle based on classical dynamics simulations over several nanoseconds.

Keywords: machine learning, platinum potential, GAP, SOAP

I. INTRODUCTION

Platinum belongs to the noble metal family and is often used in expensive jewelry. But the wider importance of Pt for the global economy stems from its countless industrial uses, even in elemental crystalline form. Platinum is commonly used as a catalyst for many chemical reactions. For instance, Pt is the best known catalyst for the hydrogen evolution reaction (HER), where it shows an extremely small overpotential [1, 2]. Pt is also one of the few catalysts that can withstand the highly oxidizing environments of the oxygen reduction reaction (ORR) and oxygen evolution reaction (OER) [3, 4]. At the same time, Pt is scarce in the Earth's crust, and its supply for industrial applications is severely limited by cost and availability. Still, for some applications, the use of Pt can be so advantageous compared to the next-best option, that it remains in wide use. To reduce the amount of raw Pt that is needed for a given application, Pt thin films or nanoparticles (NPs) can be used instead of the bulk material. The catalytic properties of Pt films are strongly influenced by crystallographic surface orientation [2]; for NPs, size and shape are the parameters that determine these properties [5–7]. Understanding the atomic-scale structure of such systems is, therefore, critical for understanding the catalytic properties.

In this article, we introduce and validate a general-purpose machine learning (ML)-based Gaussian approximation potential (GAP) [8, 9] for elemental Pt. This potential offers similar accuracy as density-functional theory (DFT) for a small fraction of the computational cost. Our potential shows extremely good transferability, accurately predicting the interatomic interactions in Pt from bulk to surface through NPs. The paper is organized as follows. We first discuss the GAP theoretical framework and the generation of training data. We then benchmark our potential against the prediction of the basic material properties of bulk, surface and NP platinum. Finally, we use the GAP to compute the pressure-temperature phase diagram of Pt using the nested sampling (NS) method and to study the nucleation of face-centered cubic (FCC) Pt during the solidification of a large Pt NP.

II. METHODS

A. Gaussian approximation potentials

Gaussian approximation potentials use kernel-based ML techniques to regress the potential energy surface (PES) of an atomistic system. Provided atomic data is available (typically energies, forces and virials), usually computed at the DFT level of theory, a GAP can be *trained* on that data, from which it *learns*. A GAP prediction is made by comparing the atomic structure for which we seek the prediction to a set of structures in the database. Each of these comparisons yields a *kernel*, or measure of similarity, which is bounded between 0 (the two structures are nothing alike) and 1 (the structures are identical). Different *descriptors*, and combinations thereof, of the atomic structure can be used to describe the atomic environments. For instance, in this work we use a combination of two-body (2b) and many-body (mb) `soap_turbo` descriptors [10, 11]. The actual pre-

diction for the local atomic energy of atom i is expressed as:

$$\bar{\epsilon}_i = e_0 + (\delta^{(2b)})^2 \sum_s \alpha_s^{(2b)} k^{(2b)}(i, s)$$
$$+ (\delta^{(mb)})^2 \sum_s \alpha_s^{(mb)} k^{(mb)}(i, s), \qquad (1)$$

where $k(i, s)$ is the kernel between the atomic environment of i and the different atomic environments s in the *sparse set* (a subset of structures in the training database), the α_s are fitting coefficients obtained during training, e_0 is a constant energy per atom and δ gives the energy scale of the model. Forces can be obtained analytically from the derivatives of Eq. (1). More details about the GAP framework and many-body descriptors are given in Refs. [8–11].

We generate training data at the DFT level using the PBE functional approximation [12] and will denote it as PBE-DFT from now on. We use a highly converged plane-wave basis set with a 520 eV cutoff and an adaptive reciprocal-space integration mesh such that the number of $\mathbf{k}$ points is given by $N_{\mathbf{k}} = 1000/N_{\text{atoms}}$. The VASP software [13–15] is used with input options given in the appendix. The composition and generation of the database are discussed in Sec. II B. The training and validation of the potential are done with the QUIP/GAP codes [16]. Structure manipulation and database sorting are done with ASE [17]. Molecular dynamics (MD) simulations are carried out using LAMMPS [18, 19] and TurboGAP [20].

B. Database generation and accuracy tests

We want to create a robust Pt GAP that can be used safely in exploratory work, e.g., to assess the stability of Pt NPs derived computationally. To this end, the GAP needs to be simultaneously accurate *and* transferable. Within a data-driven approach, it is important to note that prior knowledge of physics and chemistry is not embedded in the form of the potential. That is, a GAP does not "know" about the Schrödinger equation – it only knows about data it has seen during training. Therefore, the training set must be carefully crafted to contain all the relevant configurations. This includes (meta)stable structures, but also, perhaps counterintuitively, high-energy structures. High-energy structures must be present in the database so that the GAP learns that they are, in fact, of high energy, otherwise the GAP could spuriously predict previously unseen unstable structures to be low in energy.

It is also useful to realize that high-energy observables can be learned with less accuracy than low-energy ones, because low-energy structures contribute much more to the partition function of the system at the temperatures

of interest, and thus to the derived thermodynamic properties. This leads to an efficient database construction strategy where a few disordered structures, such as high-temperature liquid or dimers at close range, are added to sample configuration space sparsely but comprehensively. Further to these, many configurations close to the known stable structures, like close-packed crystal lattices and surfaces thereof, are added by "rattling" the atoms around equilibrium and applying small amounts of strain to the periodic cells. This, in turn, begs the question: what about the *unknown* stable structures?

To improve a GAP in a yet unknown region of configuration space, a successful strategy is iterative training [21]. In iterative training one trains several versions of the GAP, and each time uses the newest GAP to predict stable structures. The energy values and atomic forces for those structures are then computed with PBE-DFT and fed to the next version of the GAP, which will learn from its predecessor's successes and, especially, failures. This iterative procedure progressively refines the GAP's accuracy in the region of configuration space where the target structures (e.g., NPs) reside. The advantage is that the computationally demanding procedure, the structure generation, which might require thousands or millions of energy and force evaluations, is performed with the GAP, inexpensively. The PBE-DFT calculations are only carried out for the final structures or, in some cases, a small subset of the structures selected along the path followed in configuration space to generate the final ones.

Figure 1 shows the most commonly used numerical benchmark for machine learning potentials (MLPs), i.e., a scatterplot of predicted versus reference energies for a 20%/80% test/training sets split. That is, out of the entire database of structures, 80% are used to train the GAP and the 20% unseen structures are used to test the potential outside the training set. The root mean-square error (RMSE) is computed to give a single numerical score for the overall performance of the potential. Our Pt GAP shows remarkably low errors in this simple test, with an RMSE of only 1.6 meV/atom. Application-specific tests of the GAP are presented in the following section, more indicative of how this potential performs for large-scale and high-throughput simulations.

In Fig. 1 we also show the predictions of three embedded-atom method (EAM)-type potentials on our test set for comparison: Zhou's EAM [22, 23], the Gupta potential [24] and Lee's modified EAM (MEAM) [25]. EAM-type potentials are usually fitted using ground-state (low-temperature) experimental data. For instance, Zhou's EAM was fitted to reproduce (quoting the authors) "basic material properties such as lattice constants, elastic constants, bulk moduli, vacancy formation energies, sublimation energies, and heats of so-
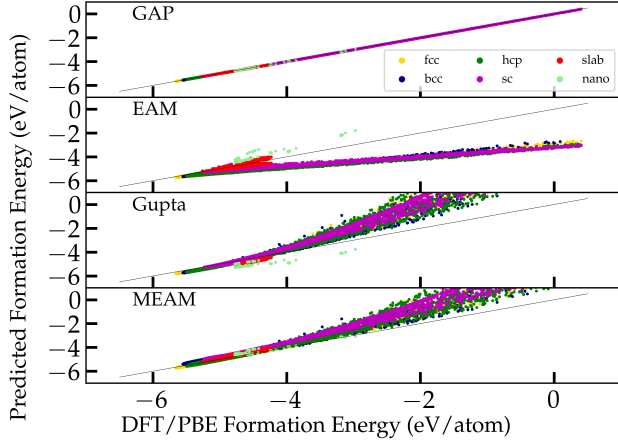
Figure 1. Validation of the Pt GAP performed on atomic configurations unseen during training. The different configuration types (FCC, HCP, etc.) are indicated with different colors. The results of testing an EAM, Gupta and MEAM potential on the same set of structures are given for reference. Formation energies are computed by $E_{\mathrm{f}} = E_{\mathrm{pred}} - n\mu$, where n gives the number of atoms in the structure and μ is the reference energy per atom for the given potential (e.g., the energy of an isolated Pt atom). The GAP errors are: maximum energy error: 0.043 eV/atom; energy RMSE: 1.6 meV/atom; and force RMSE: 0.111 eV/Å. The EAM, Gupta and MEAM errors are, respectively: maximum energy error: 3.1, 7.7 and 4.8 eV/atom; energy RMSE: 420, 1457, and 607 meV/atom; and force RMSE: 1.36, 1.69 and 1.21 eV/Å.
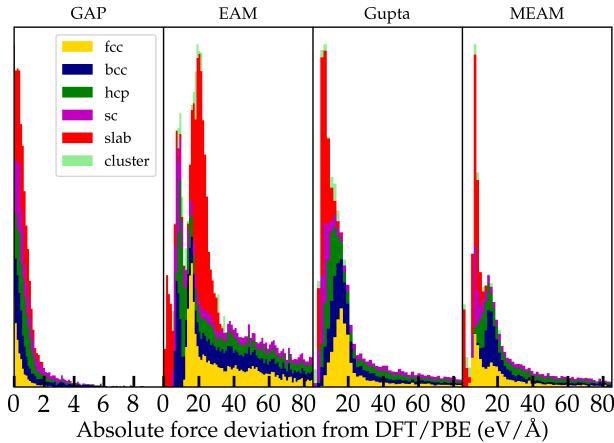

Figure 2. Force-error stacked histograms for our GAP and the tested reference potentials. Note that the ranges are one order of magnitude wider for EAM, Gupta and MEAM, compared to the GAP. The distributions are color coded according to structure type. The corresponding RMSEs are given in the caption of Fig. 1.

lution" [22]. While EAMs can satisfactorily reproduce the energetics of bulk FCC near equilibrium, as expected from the composition of their training database, all other structure types are modeled significantly less accurately. We will show in Sec. III C a further comparison for NPs. In Fig. 2 we show a histogram of force errors. Systematic deviations for the reference potentials (i.e., the error distributions peak above zero) are apparent, also visible in Fig. 1 for high-energy structures. These high-energy structures fall outside the scope of EAM-type potentials. However, they become relevant in low-dimensional systems and, e.g., at high temperature and/or pressure.

Clearly, the improved accuracy of GAP comes at the expense of additional CPU time. For instance, to perform a single-point calculation for a NP with 147 atoms, our GAP requires approximately 109 ms of CPU time whereas an EAM calculation only needs 1.2 ms. The GAP is still significantly faster than PBE-DFT (using VASP), for which this calculation requires of the order of 102 CPU hours (i.e., $\sim 3.5 \times 10^6$ times more expensive than the GAP).

C. Nested sampling

We use the nested sampling (NS) technique [26, 27] to evaluate the bulk macroscopic thermodynamic properties of the new Pt GAP model. NS samples the entire potential energy surface, starting from high-energy random configurations (representing the gas phase) down to the ground-state structure through a series of nested energy levels, without requiring any advance knowledge of the stable phases [28, 29]. A unique advantage of NS is that it allows the calculation of the partition function as a simple post-processing step. This gives access to thermodynamic properties, such as the heat capacity–which is the second derivative of the partition function with respect to temperature–and hence enables us to identify all the phase transitions of the system. In the current work we perform the NS calculations at constant pressure, to compute the pressure-temperature phase diagram [30–33]. Simulations were carried out using the pymatnest program package [34], using LAMMPS to perform the dynamics.

III. BENCHMARKS

Our Pt GAP has been designed with the goal of general applicability in mind. In this section we prove its transferability across a selection of different applications representative of common use cases. We test the GAP for basic bulk properties (equation of state, elasticity and phonons), surface energetics and NP formation energies. While avoiding a too detailed examination of
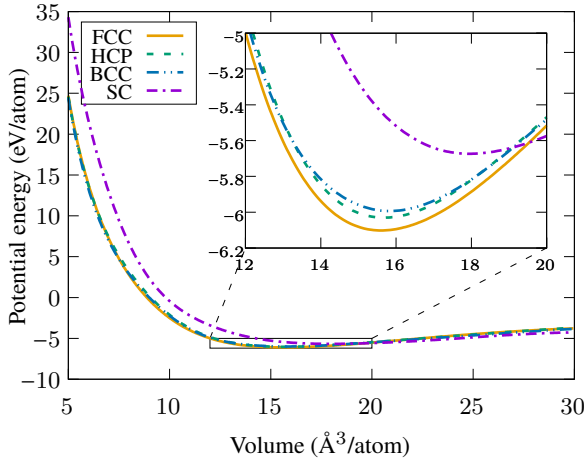
Figure 3. Equation of state for three cubic and one hexagonal Pt crystal phases: face-centered cubic (FCC), hexagonal closed-packed (HCP), body-centered cubic (BCC) and simple cubic (SC). The inset shows a closeup in the region where the global minimum is located.

each application, which could merit on their own more focused studies, these examples showcase the predictive power of the new GAP. In Sec. IV we describe two, more detailed, applied studies: the phase diagram and a spontaneous crystal nucleation in nanostructured Pt.

Accuracy tests that are missing from this section are those relevant to nanoscopic processes in surface diffusion, aggregation, nucleation and, more generally, rare events involving the description of a transition state while crossing an energy barrier. The exploration of the region of configuration space corresponding to these is difficult to automate, because transition states contribute much less to the partition function than stable states and will not be sampled by MD in significant proportions. We are currently developing the methodology to automate incorporating transition-state configurations for GAP training, and will add these to future versions of our Pt GAP as these developments become available. In the meantime, one should expect inconsistent prediction of transition-state energies with our GAP and individual calculations should be benchmarked against DFT before trusting the results.

A. Equation of state, elastic properties and phonons

The equation-of-state calculation shows the expected minimum for the FCC phase from zero up to very high pressure, with HCP about 60 meV/atom above FCC and body-centered cubic (BCC) slightly above HCP. The simple cubic (SC) phase is significantly higher in energy than FCC, HCP and BCC, except at large tensile

Table I. Comparison of GAP-predicted elastic constants with PBE-DFT as well as experimental values. The percentage in brackets shows the deviation vs experiment for PBE-DFT and EAM, and the deviation vs PBE-DFT for GAP.

	Exp. [36]	PBE-DFT	GAP	EAM
C_{11} (GPa)	373	320 (-14%)	333 ($+4\%$)	345 (-8%)
C_{12} (GPa)	242	218 (-10%)	228 ($+5\%$)	250 ($+3\%$)
C_{44} (GPa)	78	77 (-1%)	80 ($+4\%$)	76 (-3%)

strain, i.e., at large (and unrealistic) negative pressures, where it becomes the stable phase. All phases evolve smoothly as a function of unit cell volume, as shown in Fig. 3.

Our tests for Pt show that phonons and elastic constants can be learned accurately when the training data only contains structures created for this specific purpose. However, the trained potential is then only able to describe those properties, and will not have general-purpose applicability. When different structures are added to bring in more general-purpose applicability, the high accuracy on both phonons and elastic constants is sacrificed. Phonons (Fig. 4) are still described reasonably well as compared to PBE-DFT results as far as the main trends are concerned, except for a systematic deviation at the W point. Table I shows the elastic constants computed with GAP and compared to PBE-DFT, as well as to experiment. Overall, the agreement with PBE-DFT (the GAP's "ground truth") is good, with a systematic deviation of only $+4\%$. This deviation is smaller than the PBE-DFT error as compared to experiments, highlighting how, in some cases, the overall accuracy of the GAP is more limited by the intrinsic accuracy of the reference method (PBE-DFT in our case) than by the accuracy of the fit. That is, for the specific purpose of calculating elastic constants, the GAP is a better representation of PBE-DFT than PBE-DFT is of reality. For reference, we also provide the elastic constants computed with EAM, which compare favorably to experiment. They are indeed closer to the experimental values than the PBE-DFT results, a consequence of the fact that the EAM was fitted to reproduce experimental ground-state results, as discussed earlier.

B. Surfaces

Platinum is a material widely used in interfacial (electro)catalysis, and thus it is important to ensure that an interatomic potential for Pt can accurately reproduce surface formation energies. The three surfaces most commonly studied are those defined by the (111), (100)
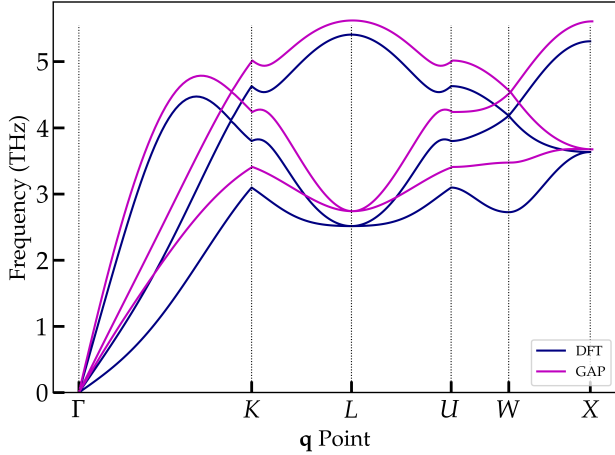
Figure 4. Phonon dispersion as computed by GAP and PBE-DFT with phonopy [35]. The trends are well reproduced in comparison to PBE-DFT except for a systematic deviation at the W point.
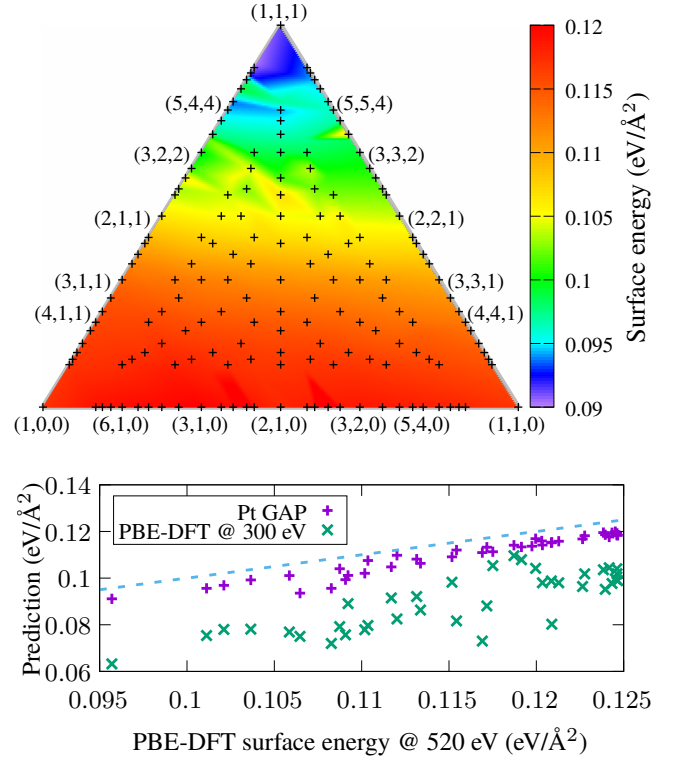

Figure 5. (Top) Surface energies computed with the Pt GAP for a range of crystal orientations resulting from tilting the faces between the (111), (100) and (110) directions. Each cross represents an actual data point, with selected Miller indices indicated, and the color map is drawn by interpolating between those. (Bottom) Comparison between the Pt GAP, a standard-quality PBE-DFT calculation (with VASP defaults and a 300 eV plane-wave cutoff), and our reference VASP PBE-DFT calculations (which use a larger cutoff of 520 eV).

and (110) crystallographic FCC planes [2]. The (111) surface is the most stable one and the one most often used in electrocatalysis, e.g., for hydrogen production, due to the low overpotential it exhibits for HER [1].

A comprehensive study of surface energetics for arbitrary Miller indices (hkl) becomes prohibitive for DFT, due to the large number of atoms in the unit cell for large indices. For example, a 7-atom thick Pt slab with $(10\,10\,10)$ indices already contains 280 atoms in the *primitive* unit cell. With our Pt GAP, studying these surfaces with small tilt angles becomes possible. We therefore calculated the surface formation energies, with bulk FCC Pt as reference, for all the symmetry-inequivalent Miller planes that can be constructed in Pt when letting each index run up to 10. To ensure that reconstruction effects beyond the primitive unit cell are considered, we ran the calculation for the primitive unit cell generated with ASE [17] as implemented by Buus, Howalt and Bligaard, its Niggli equivalent cell [37–39], as well as 2×2 supercells built thereof. We included small random initial displacements of the atoms to avoid biasing the geometry optimization due to high-symmetry starting configurations. Altogether, six calculations were carried out for each set of Miller indices and the obtained surface formation energies per atom were always the same (except for negligible numerical differences). This indicates that simple relaxation of the atomic positions takes place as the surfaces are created and that the surfaces have the same periodicity as the primitive unit cell.

Figure 5 (top panel) shows the surface formation energies for varying Miller indices within the triangle enclosed by the (111), (110) and (100) planes as end

points. The values predicted for those planes, 0.091, 0.117 and 0.117 eV/Å^2, respectively, are in good agreement with our reference PBE-DFT values (0.096, 0.123 and 0.120 eV/Å^2, respectively) and with recent values from the literature [40]. The GAP predicts smooth transitions as the cleaved (and relaxed) crystal facet is tilted between the most common facets. The bottom panel of the figure shows the surprising result that our Pt GAP is more capable of reproducing the PBE-DFT surface energies provided by a "high-quality" PBE-DFT calculation (computed with the same VASP settings as those reported in Sec. II) than another PBE-DFT calculation with "standard" settings. The GAP tends to slightly underestimate the surface formation energies (by about 5%) but the trends, i.e., the relative formation energies, are accurately captured.
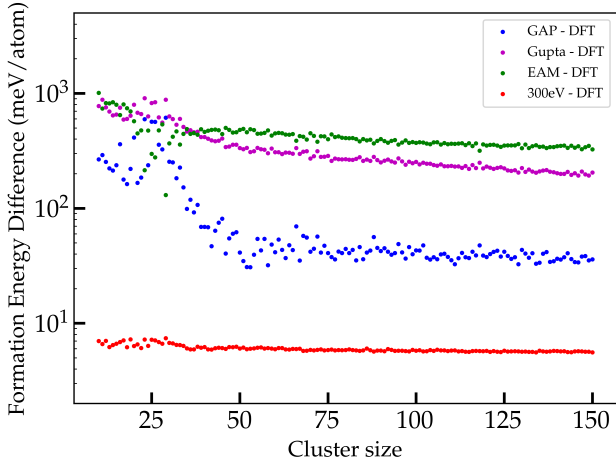
Figure 6. Formation energies for a selection of annealed NPs computed with different potentials and standard-quality PBE-DFT versus a benchmark-quality PBE-DFT calculation.

C. GAP accuracy for nanoparticle modeling

We have generated a large database of Pt NPs for this work. This database is divided into the two following subsets, NP-DB01 and NP-DB02. NP-DB01 contains 8000 NPs generated between $N_{atoms} = 10$ and $N_{atoms} = 349$ using an annealing-quenching-relaxation procedure, starting from a highly disordered precursor, where the annealing and quenching steps take 20 ps each and the annealing happens at 1500 K; we call this a "cooking" protocol. NP-DB02 contains 3400 NPs between $N_{atoms} = 10$ and $N_{atoms} = 349$ (10 for each size) where the annealing step of the cooking protocol takes place at the optimal crystallization temperature of 1150 K (see Sec. IV B) but otherwise generated in the same way as NP-DB01. This database is freely available from the Zenodo repository [41] and will be extended in subsequent work, in particular with larger NPs beyond $N_{atoms} = 349$.

To assess the ability of our GAP to accurately model Pt NPs and to compare it to previously available, commonly used, force fields for Pt modeling, we selected NPs from NP-DB01 up to $N_{atoms} = 150$. The energies were computed with our GAP, standard-quality PBE-DFT (300 eV plane-wave cutoff), the Gupta potential [24], and the EAM potential [22, 23]. We compare all these numbers to a benchmark-quality PBE-DFT calculation (520 eV plane-wave cutoff). The results of this comparison are shown in Fig. 6. Clearly, the GAP outperforms the other force fields with errors ($\sim$ 40 meV/atom) one order of magnitude smaller than Gupta ($\sim$ 400 meV/atom) and EAM ($\sim$ 500 meV/atom) around and above 50-atom NPs.

The GAP errors for these NPs are about 5 times larger than those obtained from standard-quality PBE-DFT. For very small NPs ($<$ 50 atoms) the GAP results are still better than for the other force fields but the errors are significantly higher than for larger NPs. Since the atomic motifs in small NPs look significantly different from those of bulk and surfaces, it is not surprising that the errors are larger.

The accuracy of GAP can be enhanced specifically for NPs by iteratively training the potential for that purpose. That is, we can improve the accuracy of the GAP in the future by adding (some of) these NPs to the training set and training a new version of the potential, as exemplified in Fig. 7. In that figure we observe the performance of two versions of the Pt GAP. The first one, GAPv1, is initially used to make two sets of small NPs, with $N_{atoms} \leq 50$. One of the sets is used to retrain the GAP, giving GAPv2, and the second set is used to test the predictions of both versions versus PBE-DFT. The results are shown on Fig. 7 (left) were GAPv1 is shown to predict too low (i.e., too stable) energies for the smallest NPs in the test set ($N_{atoms} \lesssim 40$) whereas GAPv2 correctly orders all of the NPs generated with GAPv1. On the right-hand side of the figure we show the energy predictions of GAPv1 and GAPv2 for NPs that were generated with GAPv2. There are two features of the GAP accuracy refinement provided by iterative training which are apparent from this right-hand panel. On the one hand, as expected, GAPv2 produces "better" NPs than GAPv1, in the sense that they are lower in energy when looking at the PBE-DFT energy prediction (i.e., the datapoints are shifted horizontally to the left, compared to the left-hand panel), and there is less data scatter. On the other hand, counterintuitively, the GAPv1 predictions for these GAPv2-generated NPs are in better agreement with PBE-DFT than the GAPv2 predictions. While unexpected, this is a typical result for early iterations in GAP iterative training: a given iteration of the potential, used in an application-specific simulation, will favor structures which populate artificially low regions of the PES. As new iterations of the potential add these low-energy structures to the database, the PES is refined and the GAP "unlearns" the spurious minima and the scatterplot converges towards optimal agreement with DFT.

The structure generation strategy that we followed here to augment the GAPv1 database is as follows. We first generate all the regular FCC tetrahedra that can be constructed below 50 atoms, which correspond to 4, 10, 20 and 35 atoms. We then start an MD simulation from the ideal (relaxed) structure, quickly (10 ps) heat up to 3000 K and quickly (another 10 ps) quench down to 100 K. From this MD trajectory, we sample 11 equidistant (in time) snapshots, which ensures we incorporate a wide diversity of small nanoclusters, including some that are high in energy: regular (crystal-
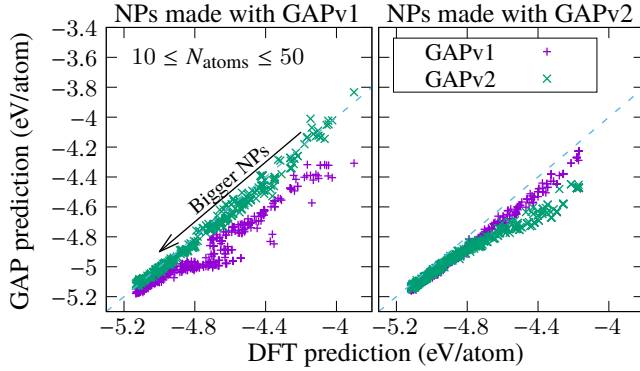
Figure 7. (Left) Predicted GAPv1 and GAPv2 energies computed on NPs generated with GAPv1, versus the corresponding DFT values, for NPs in the size range from 10 to 50 atoms. High energy-per-atom values correspond to smaller NPs whereas low values correspond to larger NPs. (Right) Same test as on the left panel but performed on NPs generated with GAPv2. The followed NP generation method in both cases is the "cooking" protocol reported in the text.

like), thermally disordered and quenched structures are added to the training database.

Generally, as new training configurations are generated, we can retrain and refine the accuracy of our GAP. For reference, we provide in the repository [42] two versions of the GAP: the one used for most of the simulations presented in this article (v1) and the one that contains a small amount of NP-specific iterative training (v2). Any future version of the GAP will be added to this repository together with a note on any further additions to the database, compared to the configurations reported here, with all published versions remaining publicly available. This will ensure that the user base of the potential has easy access to the most accurate (and most recent) Pt GAP while enabling reproducibility of the results produced with all earlier versions. Upcoming work from our group will focus on a detailed study of small Pt NP formation and stability, and we expect to update this repository with a NP-optimized version of the GAP in the near future.

For the sake of clarity, we emphasize here that GAPv1 was used to generate all the results in this paper except for those labeled as GAPv2 results in this subsection. In addition, we note that the linked repository [42] allows to browse the full history of GAP versions, even though the latest version is shown by default. Both v1 and v2 can be retrieved from the repository and are listed under "Versions".

IV. APPLICATIONS

A. Pressure-temperature phase diagram

The NS calculations were performed as presented in Ref [31]. The simulations were run at constant pressure in the range of $p = 0.07 - 50$ GPa, using a simulation cell of variable shape and size, containing 24 atoms. We used 1000 walkers and performed 440 steps (8:1:2:2 ratio of total-energy Hamiltonian Monte Carlo, volume, cell shear and cell stretch steps) to generate the new configurations during the NS iterations. These parameters ensure convergence of the melting transition within ± 40 K. The use of small systems will inevitably cause some finite-size effects, for example an underestimation of the boiling curve and an overestimation of the melting line as compared to the macroscopic value [30]. In order to estimate this error, we repeated the simulations with 48 atoms at $p = 1$ GPa, and obtained 2.8% lower melting temperature as compared to the 24-atom calculation.

Figure 8 shows the pressure-temperature phase diagram. At low pressure, we observe a heat capacity peak at high temperature corresponding to the boiling curve and its extension to the supercritical region, the Widom line, marked by a shallower and broader peak (shown by dashed red line in Fig. 8). To locate the critical point in the NS calculations, we drew on the results of Bruce and Wilding [43] and calculated the density distribution in the temperature region of the peak. With this, we estimate the critical parameters to be $p_c = 0.1 - 0.2$ GPa and $T_c = 9500 - 10600$ K. The low-pressure melting transition is estimated to be ≈ 1650 K, hence underestimating the experimentally determined transition. This inaccuracy could be either due to our GAP or to an inherent error of the PBE functional used to train it. Since NS calculations at the PBE level are simply intractable, there is no straightforward way to pinpoint the origin of this disagreement with experiment. The NS calculations found the solid structure to be FCC as expected, and explored other close-packed stacking variants only in thermodynamically insignificant proportions.

B. Spontaneous FCC nucleation and crystallization

We also used the Pt GAP to study the spontaneous nucleation of the stable FCC structure and the spontaneous formation of facets in a large NP (16384 atoms) with MD. Figure 9 shows the sequence from the initial cube carved out of an FCC lattice. This is melted at 3000 K for 40 ps and then the quenching process takes place by cooling the NP from 3000 K down to 300 K
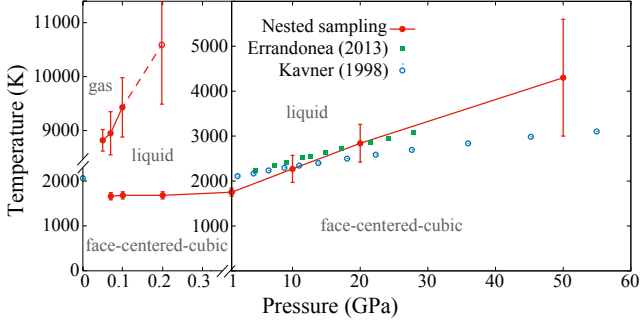
Figure 8. Pressure-temperature phase diagram calculated by nested sampling (red lines and symbols). Error bars represent the full widths at half maximum of the heat capacity curves. Green and blue symbols show experimental melting temperatures taken from Refs. [44] and [45], respectively.

over 1 ns using a linear temperature profile, controlled by a Berendsen thermostat with time constant 0.1 ps. The figure also shows a slice through the middle of the NP and, for reference, a periodic solid with the same number of atoms and undergoing the same temperature profile. For the solid, the pressure is controlled with a Berendsen barostat with time constant 1 ps and inverse compressibility equal to 100 times that of water.

To get further insight into the atomistic processes taking place during crystallization, in Fig. 9 we map the similarity of the local atomic structures to reference atomic motifs: bulk FCC and the stable (100), (110) and (111) FCC surface reconstructions. This is done by computing the SOAP descriptors of each atom in the system and calculating the similarity kernel with the SOAP descriptors of the reference motifs. These similarities are indicated by color coding the resulting structures. As expected, towards the end of the quench the interior of the NP (as well as the solid) is FCC-like, and the NP facets are (111)-like. Interestingly, the simulation shows that the formation of the FCC interior is nucleated from the surfaces inwards. Therefore, there is grain formation with the (111) direction pointing approximately from the surface towards the center of the NP. For this reason, the resulting NP is polycrystalline, with the grain boundaries indicated by dark-colored atoms. It is clear from the figure that the formation of the FCC interior in the NP happens at a *higher* temperature than in the solid due to the nucleation effect at the (111) facets. A video animation of this process is available [46].

To elucidate the role of quench rate on the results, we monitored the evolution of the NP's structure as it was cooled down from 3000 K to 300 K for additional quench rates corresponding to 2 ns to 10 ns simulations, with the same MD settings as before. Figure 10 shows the evolution of the potential energy as a function of tem-
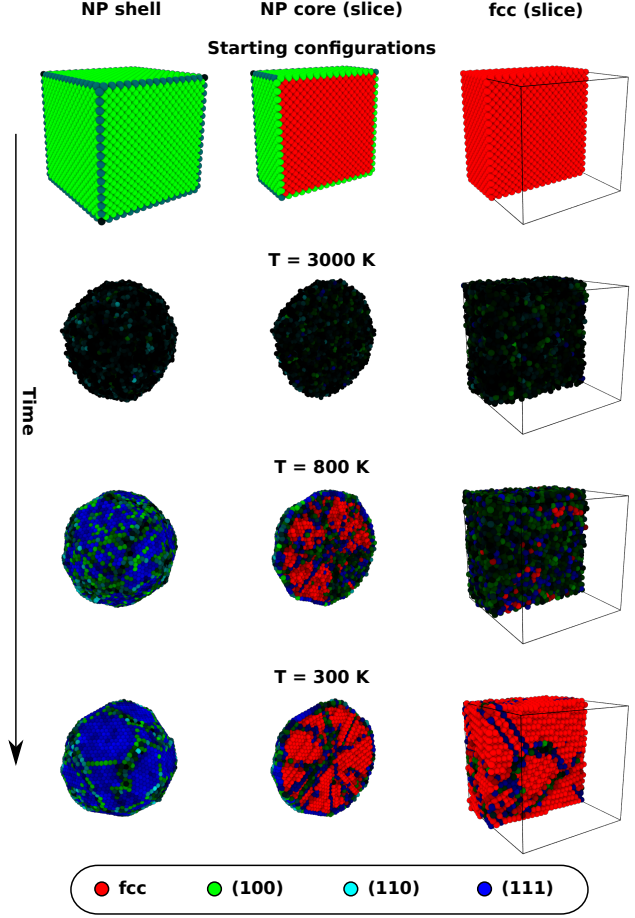

Figure 9. Snapshots throughout the process of spontaneous crystallization from a melted Pt droplet as it cools down to room temperature, as modeled with our GAP. The left column shows the resulting NP from the outside, whereas the central column shows a slice through the middle. The same process for bulk Pt is shown on the right column. The color coding indicates the degree of similarity, computed from SOAP kernels, of each local atomic environment (centered on the atoms) to the stable bulk FCC motif, as well as the three most common surface motifs: (100), (110) and (111), where (111) is the most stable facet. The dark bands between FCC (red) regions in the final structures correspond to grain boundaries.

perature in the 1400 K to 800 K temperature window, where most of the FCC nucleation takes place in these simulations (outside of this range the potential energy evolves linearly with temperature, as expected from the virial theorem). According to our MD results, the onset of significant structure rearrangement favorable towards FCC nucleation takes place at around 1200 K and continues down to a temperature which depends on the quench rate (the slower the rate the higher the final temperature). From these values we infer an optimal crystallization temperature around 1150 K. This
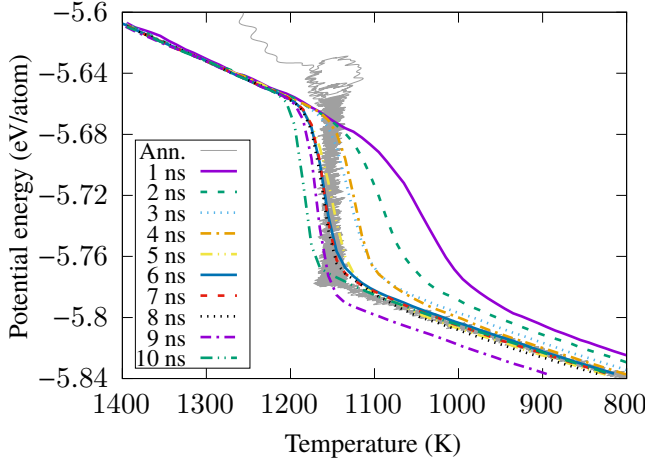
Figure 10. Potential energy profile as a function of temperature in a series of melt-quench simulations, for different cooling rates (1 ns to 10 ns cooling period). The overall process starts at 3000 K and ends at 300 K; the shown data focuses on the region where crystallization takes place, corresponding to the formation of stable FCC motifs. The thin gray line shows the profile of a simulation where the sample is quenched extremely fast from 3000 K to 1150 K and annealed at that temperature before being brought down to room temperature. See text for details.

is analogous to the graphitization temperature in carbon materials [47, 48]. We therefore repeated the MD simulation starting from the 3000 K melted NP but fixing the thermostat's target temperature at 1150 K and annealed for 1 ns (indicated as "Ann." in the figure). There is a rapid quench from 3000 K to 1150 K and then the system equilibrates for a few ps, corresponding to the loop seen at high potential energy, before it starts to go down in energy as it crystallizes (the vertical drop in potential energy at 1150 K). Most of the annealing process was completed after 250 ps, with no noticeable further drop in potential energy after 500 ps of MD. After the 1 ns annealing simulation had ended, we further quenched the structure to 300 K over 100 ps using a linear temperature profile. The results showed good agreement with the more computationally demanding slow quenches. This annealing process at 1150 K thus allows us to minimize the number of MD steps that are required to generate a reasonably stable NP, generated from a process mimicking spontaneous solidification.

V. CONCLUSIONS AND OUTLOOK

We have developed a GAP for Pt with state-of-the-art force-field accuracy for the description of bulk, surface and nanostructured systems. We have benchmarked our GAP against PBE-DFT for general accuracy, elasticity,

phonons, surface energetics and NP formation energies. Except for small NPs ($N_{atoms} \lesssim 40$), our GAP shows remarkable agreement with the reference PBE-DFT data. We have then proceeded to use the GAP in situations beyond the reach of PBE-DFT calculations. Namely, we have computed the temperature-pressure phase diagram and studied the spontaneous solidification and FCC-motif nucleation in a large NP. The new GAP and several other resources have been made freely available. In the near future, we will further develop our reference database and the potential itself for improved description of NPs and surface dynamics, with the objective to get detailed insight into the atomic-scale phenomena taking place in Pt-based systems of interest in (electro)catalysis.

Appendix A: VASP input file

The VASP INCAR input file used for the PBE-DFT calculations is given below:

```
PREC = Accurate
ENCUT = 520
EDIFF = 1.0e-05
ISMEAR = 0; SIGMA = 0.1
ALGO = Normal
LWAVE = .FALSE.
LCHARG = .FALSE.
```

The k-space sampling is not explicitly set in the INCAR file. Instead, **k** points are chosen by homogeneously sampling the first Brillouin zone with the total number of points determined by the relation $n_{atoms} \times n_{\mathbf{k}} = 1000$. To enable high-throughput calculations, the Fireworks framework [49] was used for task automation and single-point workflows, similar to the implementation in Atomate [50], which rely on Custodian [51] as VASP handler.

[1] J. Solla-Gullón, P. Rodríguez, E. Herrero, A. Aldaz, and J. M. Feliu, "Surface characterization of platinum electrodes," Phys. Chem. Chem. Phys. **10**, 1359 (2008).

[2] N. Garcia-Araez, V. Climent, and J. M. Feliu, "Analysis of temperature effects on hydrogen and OH adsorption on Pt(111), Pt(100) and Pt(110) by means of Gibbs thermodynamics," J. Electroanal. Chem. **649**, 69 (2010).

[3] J. K. Nørskov, J. Rossmeisl, A. Logadóttir, L. R. K. J. Lindqvist, J. R. Kitchin, T. Bligaard, and H. Jónsson, "Origin of the overpotential for oxygen reduction at a fuel-cell cathode," J. Phys. Chem. B **108**, 17886 (2004).

[4] I. E. L. Stephens, A. S. Bondarenko, U. Grønbjerg, J. Rossmeisl, and I. Chorkendorff, "Understanding the electrocatalysis of oxygen reduction on platinum and its alloys," Energ. Environ. Sci. **5**, 6744 (2012).

[5] C. Wang, H. Daimon, T. Onodera, T. Koda, and S. Sun, "A general approach to the size-and shape-controlled synthesis of platinum nanoparticles and their catalytic reduction of oxygen," Angew. Chem. **120**, 3644 (2008).

[6] C. M. Sánchez-Sánchez, J. Solla-Gullón, F. J. Vidal-Iglesias, A. Aldaz, V. Montiel, and E. Herrero, "Imaging structure sensitive catalysis on different shape-controlled platinum nanoparticles," J. Am. Chem. Soc. **132**, 5622 (2010).

[7] E. Skúlason, A. A. Faraj, L. Kristinsdóttir, J. Hussein, A. Garden, and H. Jónsson, "Catalytic activity of Pt nano-particles for H_2 formation," Top. Catal. **57**, 273 (2014).

[8] A. P. Bartók, M. C. Payne, R. Kondor, and G. Csányi, "Gaussian approximation potentials: The accuracy of quantum mechanics, without the electrons," Phys. Rev. Lett. **104**, 136403 (2010).

[9] A.P. Bartók and G. Csányi, "Gaussian approximation potentials: A brief tutorial introduction," Int. J. Quantum Chem. **115**, 1051 (2015).

[10] A. P. Bartók, R. Kondor, and G. Csányi, "On representing chemical environments," Phys. Rev. B **87**, 184115 (2013).

[11] M. A. Caro, "Optimizing many-body atomic descriptors for enhanced computational performance of machine learning based interatomic potentials," Phys. Rev. B **100**, 024112 (2019).

[12] J. P. Perdew, K. Burke, and M. Ernzerhof, "Generalized gradient approximation made simple," Phys. Rev. Lett. **77**, 3865 (1996).

[13] G. Kresse and J. Furthmüller, "Efficient iterative schemes for *ab initio* total-energy calculations using a plane-wave basis set," Phys. Rev. B **54**, 11169 (1996).

[14] G. Kresse and D. Joubert, "From ultrasoft pseudopotentials to the projector augmented-wave method," Phys. Rev. B **59**, 1758 (1999).

[15] P. E. Blöchl, "Projector augmented-wave method," Phys. Rev. B **50**, 17953 (1994).

[16] (), https://libatoms.github.io.

[17] A. Larsen, J. Mortensen, J. Blomqvist, I. Castelli, R. Christensen, M. Dulak, J. Friis, M. Groves, B. Hammer, C. Hargus, E. Hermes, P. Jennings, P. Jensen, J. Kermode, J. Kitchin, E. Kolsbjerg, J. Kubal, K. Kaasbjerg, S. Lysgaard, J. Maronsson, T. Maxson, T. Olsen, L. Pastewka, A. Peterson, C. Rostgaard, J. Schiøtz, O. Schütt, M. Strange, K. Thygesen, T. Vegge, L. Vilhelmsen, M. Walter, Z. Zeng, and K. W. Jacobsen, "The Atomic Simulation Environment – A Python library for working with atoms," J. Phys.: Condens. Matter **29**, 273002 (2017).

[18] S. Plimpton, "Fast parallel algorithms for short-range molecular dynamics," J. Comput. Phys. **117**, 1 (1995).

[19] (), http://lammps.sandia.gov.

[20] M. A. Caro, "TurboGAP website and online documentation," http://turbogap.fi (accessed August 8, 2022).

[21] V. L. Deringer and G. Csányi, "Machine learning based interatomic potential for amorphous carbon," Phys. Rev. B **95**, 094203 (2017).

[22] X.W. Zhou, H.N.G. Wadley, R.A. Johnson, D.J. Larson, N. Tabat, A. Cerezo, A.K. Petford-Long, G.D.W. Smith, P.H. Clifton, R.L. Martens, and T.F. Kelly, "Atomic scale structure of sputtered metal multilayers," Acta Materialia **49**, 4005–4015 (2001).

[23] X. W. Zhou, R. A. Johnson, and H. N. G. Wadley, "Misfit-energy-increasing dislocations in vapor-deposited cofe/nife multilayers," Phys. Rev. B **69**, 144113 (2004).

[24] Lauro Oliver Paz-Borbón, Thomas V. Mortimer-Jones, Roy L. Johnston, Alvaro Posada-Amarillas, Giovanni Barcaro, and Alessandro Fortunelli, "Structures and energetics of 98 atom pd–pt nanoalloys: potential stability of the leary tetrahedron for bimetallic nanoparticles," Phys. Chem. Chem. Phys. **9**, 5202–5208 (2007).

[25] B.-J. Lee, J.-H. Shim, and M. I. Baskes, "Semiempirical atomic potentials for the fcc metals Cu, Ag, Au, Ni, Pd, Pt, Al, and Pb based on first and second nearest-neighbor modified embedded atom method," Phys. Rev. B **68**, 144112 (2003).

[26] J. Skilling, "Bayesian inference and maximum entropy methods in science and engineering," in *AIP Conference Proceedings*, Vol. 735 (2004) p. 395.

[27] Greg Ashton, Noam Bernstein, Johannes Buchner, Xi Chen, Gábor Csányi, Farhan Feroz, Andrew Fowlie, Matthew Griffiths, Michael Habeck, Will Handley, Edward Higson, Michael Hobson, Anthony Lasenby, David Parkinson, Livia B. Pártay, Matthew Pitkin, Doris Schneider, Leah South, Joshua S. Speagle, John Veitch, Philipp Wacker, David J Wales, and David Yallup, "Nested Sampling for physical scientists," Nat. Rev. Methods Primer **2**, 39 (2022).

[28] L. B. Pártay, A. P. Bartók, and G. Csányi, "Efficient sampling of atomic configurational spaces," J. Phys. Chem B **114**, 10502–10512 (2010).

[29] L. B. Pártay, G. Csányi, and N. Bernstein, "Nested sampling for materials," Eur. Phys. J. B **94**, 159 (2021).

[30] Robert J. N. Baldock, Lívia B. Pártay, Albert P. Bartók, Michael C. Payne, and Gábor Csányi, "Determining the pressure-temperature phase diagrams of

materials," Phys. Rev. B **93**, 174108 (2016).

[31] R. J. N. Baldock, N. Bernstein, K. M. Salerno, L. B. Pártay, and G. Csányi, "Constant-pressure nested sampling with atomistic dynamics," Phys. Rev. E **96**, 43311–43324 (2017).

[32] L. B. Pártay, "On the performance of interatomic potential models of iron: comparison of the phase diagrams," Comput. Mater. Sci **149**, 153–157 (2018).

[33] Jordan Dorrell and Livia B. Pártay, "Pressure–Temperature Phase Diagram of Lithium, Predicted by Embedded Atom Model Potentials," J. Phys. Chem. B **124**, 6015–6023 (2020).

[34] Noam Bernstein, Robert J. N. Baldock, Livia B. Pártay, James R. Kermode, Thomas D. Daff, Albert P. Bartók, and Gábor Csányi, "pymatnest," `https://github.com/libAtoms/pymatnest` (2016).

[35] A Togo and I Tanaka, "First principles phonon calculations in materials science," Scr. Mater. **108**, 1–5 (2015).

[36] S. M. Collard and R. B. McLellan, "High-temperature elastic constants of platinum single crystals," Acta Metall. Mater. **40**, 699 (1992).

[37] P. Niggli, "Krystallographische und strukturtheoretische Grundbegriffe. Handbuch der Experimentalphysik," Geol. Foren. Stock. For. **51**, 122 (1929).

[38] I. Křivỳ and B. Gruber, "A unified algorithm for determining the reduced (Niggli) cell," Acta Crystallogr. A-Cryst. **32**, 297 (1976).

[39] R. W. Grosse-Kunstleve, N. K. Sauter, and P. D. Adams, "Numerically stable algorithms for the computation of reduced unit cells," Acta Crystallogr. A **60**, 1 (2004).

[40] R. Tran, Z. Xu, B. Radhakrishnan, D. Winston, W. Sun, K. A. Persson, and S. P. Ong, "Surface energies of elemental crystals," Sci. data **3**, 1 (2016).

[41] Jan Kloppenburg and M. A. Caro, "Platinum nanoparticle database," Zenodo (2022), DOI:10.5281/zenodo.7415542.

[42] Jan Kloppenburg and M. A. Caro, "General-purpose GAP potential for platinum," Zenodo (2022),

[43] A. D. Bruce and N. B. Wilding, Phys. Rev. Lett. **68**, 193 (1992).

[44] D. Errandonea, "High-pressure melting curves of the transition metals cu, ni, pd, and pt," Phys. Rev. B **87**, 054108 (2013).

[45] A. Kavner and R. Jeanloz, "High-pressure melting curve of platinum," J. Appl. Phys. **83**, 7553–7559 (1998).

[46] M. A. Caro, "Spontaneous crystallization of a large Pt nanoparticle," Zenodo (2022), DOI:10.5281/zenodo.7415631.

[47] C. de Tomas, A. Aghajamali, J. L. Jones, D. J. Lim, M. J. López, I. Suarez-Martinez, and N. A. Marks, "Transferability in interatomic potentials for carbon," Carbon **155**, 624 (2019).

[48] Y. Wang, Z. Fan, P. Qian, T. Ala-Nissila, and M. A. Caro, "Structure and pore size distribution in nanoporous carbon," Chem. Mater. **34**, 617 (2022).

[49] A. Jain, S. P. Ong, W. Chen, B. Medasani, X. Qu, M. Kocher, M. Brafman, G. Petretto, G.-M. Rignanese, G. Hautier, D. Gunter, and K. A. Persson, "FireWorks: a dynamic workflow system designed for high-throughput applications," Concurr. Comp.: Pract. E. **27**, 5037 (2015).

[50] K. Mathew, J. H. Montoya, A. Faghaninia, S. Dwarakanath, M. Aykol, H. Tang, I.-H. Chu, T. Smidt, B. Bocklund, M. Horton, J. Dagdelen, B. Wood, Z.-K. Liu, J. Neaton, S. P. Ong, K. Persson, and A. Jain, "Atomate: A high-level interface to generate, execute, and analyze computational materials science workflows," Comput. Mater. Sci. **139**, 140 (2017).

[51] S. P. Ong, W. D. Richards, A. Jain, G. Hautier, M. Kocher, S. Cholia, D. Gunter, V. L. Chevrier, K. A. Persson, and G. Ceder, "Python Materials Genomics (pymatgen): A robust, open-source python library for materials analysis," Comput. Mater. Sci. **68**, 314 (2013).

DOI:10.5281/zenodo.7415219.